JPE 13-5-9

http://dx.doi.org/10.6113/JPE.2013.13.5.814

Uncertainty Modeling and Robust Control for LCL Resonant Inductive Power Transfer System

Xin Dai†, Yang Zou*, and Yue Sun*

†*College of Automation, Chongqing University, Chongqing, China

Abstract

The LCL resonant inductive power transfer (IPT) system is increasingly used because of its harmonic filtering capabilities, high efficiency at light load, and unity power factor feature. However, the modeling and controller design of this system become extremely difficult because of parameter uncertainty, high-order property, and switching nonlinear property. This paper proposes a frequency and load uncertainty modeling method for the LCL resonant IPT system. By using the linear fractional transformation method, we detach the uncertain part from the system model. A robust control structure with weighting functions is introduced, and a control method using structured singular values is used to enhance the system performance of perturbation rejection and reference tracking. Analysis of the controller performance is provided. The simulation and experimental results verify the robust control method and analysis results. The control method not only guarantees system stability but also improves performance under perturbation.

Key words: Generalized state space averaging, Inductive power transfer, LCL, Robust, Uncertainty

I. INTRODUCTION

Inductive power transfer (IPT) technology is a novel technology that can provide wireless energy transmission from the power supply to the electrical equipment with the aid of magnetic coupling [1], [2]. Without direct electrical contact, power transmission becomes more convenient, more robust, and more flexible. Most importantly, power transmission becomes safe [3]. Therefore, this technology can be used in harsh environments, such as underwater, explosive, and corrosive areas [4], [5]. Owing to these distinguished features, this technology has gained many successful applications in material handling system, electrical vehicle, medical implants, and consumer devices [6]–[8].

In a typical IPT system, two types of resonant converters are usually used to produce transformation from DC to high-frequency AC current, namely, series and parallel resonant converters. For the series resonant type, the resonant current flowing through the switching devices produces unnecessary power loss. Furthermore, under light-load condition, a large resonant current exists in the resonant tank and causes low efficiency. The parallel resonant converter normally requires a large DC inductor to produce a quasi-current source. The LCL resonant converter has been proposed because of the defects of these two converters. The composite resonant network exhibits great filtering capabilities. The impedance transformation feature guarantees unity power factor and high efficiency under light-load condition [9]. Furthermore, the LCL network provides high power capability and stable resonant current output.

Although an LCL converter has many advantages, its modeling and controller design remains a problem. The additional LCL tank increases the entire system orders to seven or even higher. The high-order, switching nonlinearity, parameter uncertainty, and multi-operating points make the system behavior complex and hard to model [10]. Current modeling methods can be divided into two types on the basis of the recent research on the IPT system. The first is the discrete time-mapping modeling method [11]. This modeling method sets up piecewise mapping functions of the system dynamics and integrates dynamic boundary condition solving to obtain an accurate system model. This system model can give a complete description for not only the steady state but also the transient process. However, this model requires dynamic numeric

Manuscript received Aug. 28, 2012; revised Jun. 4, 2013
Recommended for publication by Associate Editor Tae-Woong Kim.
†Corresponding Author: toybear@vip.sina.com
Tel: +86-23-65112750, Fax: +86-23-65111221, Chongqing University
*College of Automation., Chongqing University, China

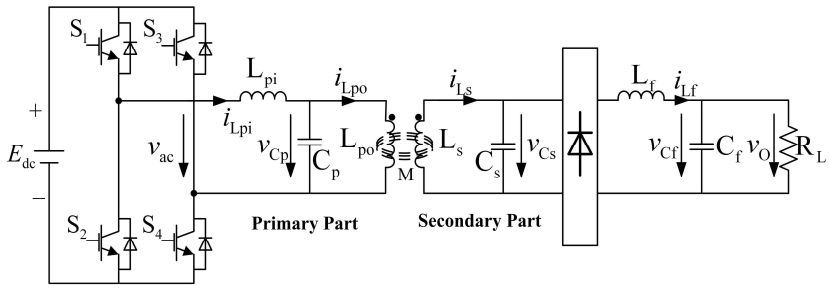

Fig. 1. LCL-resonant IPT system topology.

computing with system dynamics evolution. Given that the analytical model cannot be obtained, this model is extremely difficult for the design of the controller. The other modeling method is the generalized state space averaging (GSSA) method, which is particularly suited to full resonant converters that inherently generate quasi-sine-wave voltage and current waveforms [12]. This method transforms the nonlinear differential model in the time domain into a linear state space model in the frequency domain. The obtained system model is suited for the control design. However, all parameters must be known and fixed in the modeling process. The running frequency of an IPT system easily drifts away from the designed frequency with load variation in the system dynamics [8], [13]. Therefore, frequency and load are uncertain parameters. Involving uncertainty in the model is difficult because of the nature of modeling in the frequency domain.

Current research on the controller design of the IPT system is mainly focused on tuning-point and pick-up output voltage controls [2], [14], [15]. Bang-Bang and PID controls are two typical control methods. The distinguished feature of these methods is their independence on the system model. Moreover, these two types of controllers are easy to design and implement. However, with the development of the IPT technology, the optimal performance gradually becomes a research interest, particularly in large power capability systems such as electrical vehicles. In the controller design, a global robust controller should be considered to fulfill the requirements of not only the stability but also the optimal performance, such as perturbation rejection and fast reference tracking.

Aimed at output voltage control and performance optimization, a robust control method based on uncertainty modeling is proposed. Initially, the normal GSSA model is set up based on the differential system model. In uncertainty modeling, the frequency and load parameter uncertainties are both considered. The uncertain part is detached from the system model, and a generalized plant model is obtained via upper linear fractional transformation. A robust controller structure, including the weighting functions, is introduced. Considering the system performance, a structured singular value (SSV) is introduced to enhance perturbation rejection and reference tracking capabilities. System order reduction and discretization were performed to facilitate the control of hardware implementation. The controller performance analysis is also provided. Finally, the simulation and experimental results verify the robustness of the control method and the analysis results.

II. PRINCIPLE OF LCL-TYPE IPT SYSTEM

The topology of a typical LCL resonant IPT system is shown in Fig. 1.

The system can be divided into primary and secondary parts. The primary part comprises a full-bridge inverter and an LCL composite resonant tank. The inverter consists of four switching devices (S1–S4), which form two switching pairs (S1 and S4 and S2 and S3). The switching pairs operate complementarily and inject an approximate square wave voltage into the LCL resonant tank. The LCL resonant tank is a T-type resonant network consisting of L_{pi}, L_{po}, and C_p. The LCL network transforms the square wave voltage input into a sine current in magnetic excitation coil (L_{po}) and realizes impedance transformation to guarantee the zero-current switching (ZCS) condition. The secondary part comprises a parallel-tuned network, a rectifier, and a filter. During magnetic coupling, the pickup coil (L_s) accepts energy from the primary part and produce resonance in the parallel-tuned network to increase power transfer capacity. The load finally acquires a stable DC output with the rectifier and filter.

To reduce switching losses and Electromagnetic Interference (EMI) , two switching pairs (S1 and S4) and (S2 and S3) should be switched at zero crossing instants of the input current $i_{L_{pi}}$ of the LCL resonant tank to achieve ZCS running, as shown in Fig. 2.

The ZCS crossing detection module detects the crossing instants of input current and sends complementary driving signal to the two switching pairs to guarantee soft switching running. Under the ZCS running mode, the switching frequency keeps up with the inherent frequency variation of the LCL resonant network. Therefore, the system operation frequency drifts away from the designed frequency and

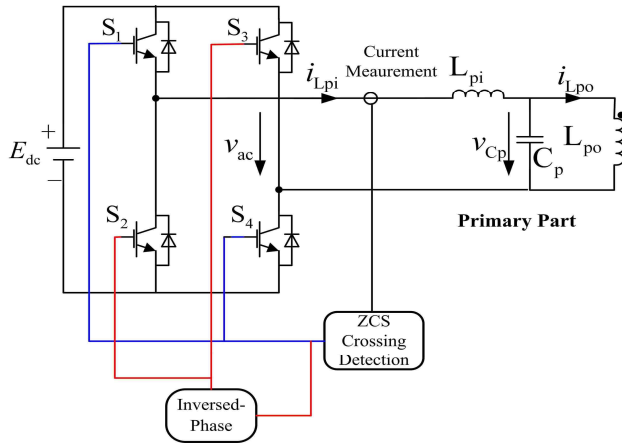

Fig. 2. ZCS running mode.

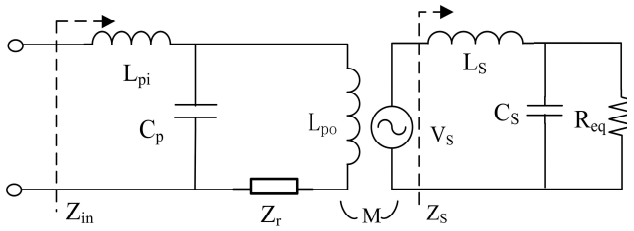

Fig. 3. Equivalent circuit of the LCL network.

becomes uncertain parameters under load variation condition. The ZCS operation condition can be acquired by the equivalent circuit (see Fig. 3).

Assuming the square wave current is drawn by the rectifier, the equivalent resistance R_{eq} of the DC part at the secondary side is provided by [16]

$$R_{eq} = \left(\pi^2 / 8\right) R_L \ . \tag{1}$$

The reflection impedance from the secondary to primary sides can be expressed by

$$Z_r = \left(\omega^2 M^2\right) / Z_S \ , \tag{2}$$

where $Z_S = j\omega L_S + R_{eq} / \left(j\omega C_S R_{eq} + 1\right)$.

The input impedance of the LCL network can be expressed as

$$Z_{in} = \frac{Z_r + j\omega L_{Lpo}}{1 + j\omega C_p \left(Z_r + j\omega L_{Lpo}\right)} + j\omega L_{Lpi} \tag{3}$$

The ZCS operation condition can be expressed as

$$\mathrm{Im}\left(Z_{in}\right) = 0 \tag{4}$$

With the implicit equation, the operation frequency ω can be solved with the numerical method.

III. GSSA Modeling

The LCL resonant IPT system is a complex system because of its switching nonlinearity, increased system order, and inconstancy of load condition. An accurate mathematical model is difficult to set up. In this paper, the GSSA method is utilized to transform the nonlinear system model in the time domain into a linear state space model in the frequency domain with the expansion of Fourier series.

According to Kirchhoff's circuit laws, the differential model of the LCL system can be obtained as

$$\begin{cases} L_{pi} i_{L_{pi}}'(t) + R_{L_{pi}} i_{L_{pi}}(t) + v_{C_p}(t) = f_p(t) E_{DC} \\ C_p v_{C_p}'(t) + i_{L_{po}}(t) = i_{L_{pi}}(t) \\ L_{po} i_{L_{po}}'(t) + R_{L_{po}} i_{L_{po}}(t) - M i_{L_s}'(t) = v_{C_p} \\ L_s i_{L_s}'(t) + R_{L_s} i_{L_s}(t) + v_{C_s} = M i_{L_{po}}'(t) \\ C_s v_{C_s}'(t) + f_s(t) i_{L_f}(t) = i_{L_s}(t) \\ L_f i_{L_f}'(t) + v_{C_f} = f_s(t) v_{C_s}(t) \\ C_f v_{C_f}'(t) + \dfrac{v_{C_f}(t)}{R_L} = i_{L_f}(t) \end{cases} , \tag{5}$$

where $R_{L_{po}}$, $R_{L_{pi}}$, and R_{L_s} are the equivalent series resistance of the inductance L_{po}, L_{pi}, and L_s, respectively.

Owing to the switching devices in the primary part and the rectifier in the secondary part, the switching nonlinear functions f_p and f_s are included in the differential equation model. The functions are used to describe the "on" and "off" state of the switching devices and can be defined as

$$f_p(t) = \begin{cases} 1 & mT < t < (2m+1)T/2, \ m \in Z \\ -1 & (2m+1)T/2 < t < (m+1)T, \ m \in Z \end{cases} , \tag{6}$$

where $f_p(t) = 1$ denotes that S1 and S4 are turned on and S2 and S3 are turned off; $f_p(t) = -1$ denotes that S2 and S3 are turned on and S1 and S4 are turned off.

As the phase difference between the input current $i_{L_{pi}}$ in the primary part and the resonant voltage v_{C_s} is 180°, the switching function $f_s(t)$ can be expressed as

$$f_s(t) = -f_p(t) \ . \tag{7}$$

Considering the differential equation model given in (5), the state vector can be defined as

$$x(t) = \left[i_{L_{pi}}(t), v_{C_p}(t), i_{L_{po}}(t), i_{L_s}(t), v_{C_s}(t), v_{L_f}(t), v_{C_f}(t)\right]^T \ . \tag{8}$$

Slow time-varying and fast oscillatory variables exist among the state variables. Given that the switching function switches its state half a period, the state variables of the resonant tank exhibits oscillation property, such as $i_{L_{pi}}, v_{C_p}, i_{L_{po}}, i_{L_s}, v_{C_s}$. However, the state variables i_{L_f}, v_{C_f} exhibit slow time-varying property because of the filter.

When the state vector $x(t)$ satisfies the Dirichlet conditions, any element of the state vector can be expanded in Fourier series as

$$x_i(t)=\sum_{-n}^{n}\langle x_i\rangle_k(t)e^{jk\omega_0 t} \tag{9}$$

where $\omega_0=2\pi/T$ is the fundamental angular frequency, k the harmonic number, and n the bound of selected harmonic number. The Fourier series coefficient can be expressed as

$$\langle x_i\rangle_k(t)=\frac{1}{T}\int_T x_i(t)e^{-jk\omega_0 t}dt \tag{10}$$

Considering the expansion of the Fourier series, the differential equation model in the time domain shown in (5) can be transformed into a generalized state variable model in the frequency domain as

$$\begin{cases}
\langle i_{\mathrm{Lpi}}\rangle_1' = -L_{\mathrm{pi}}^{-1}\left(R_{\mathrm{Lpi}}\langle i_{\mathrm{Lpi}}\rangle_1+\langle v_{\mathrm{Cp}}\rangle_1-E_{\mathrm{dc}}\langle f_{\mathrm{p}}\rangle_1\right)-j\omega_0\langle i_{\mathrm{Lpi}}\rangle_1\\
\langle v_{\mathrm{Cp}}\rangle_1' = C_{\mathrm{p}}^{-1}\left(\langle i_{\mathrm{Lpi}}\rangle_1-\langle i_{\mathrm{Lpo}}\rangle_1\right)-j\omega_0\langle v_{\mathrm{Cp}}\rangle_1\\
\langle i_{\mathrm{Lpo}}\rangle_1' = \Psi^{-1}\left(-L_{\mathrm{s}}\langle v_{\mathrm{Cp}}\rangle_1+L_{\mathrm{s}}R_{\mathrm{Lpo}}\langle i_{\mathrm{Lpo}}\rangle_1+MR_{\mathrm{Ls}}\langle i_{\mathrm{Ls}}\rangle_1+M\langle v_{\mathrm{Cs}}\rangle_1\right)\\
\qquad -j\omega_0\langle i_{\mathrm{Lpo}}\rangle_1\\
\langle i_{\mathrm{Ls}}\rangle_1' = \Psi^{-1}\left(-M\langle v_{\mathrm{Cp}}\rangle_1+MR_{\mathrm{Lpo}}\langle i_{\mathrm{Lpo}}\rangle_1+L_{\mathrm{po}}R_{\mathrm{Ls}}\langle i_{\mathrm{Ls}}\rangle_1+L_{\mathrm{po}}\langle v_{\mathrm{Cs}}\rangle_1\right)\\
\qquad -j\omega_0\langle i_{\mathrm{Ls}}\rangle_1\\
\langle v_{\mathrm{Cs}}\rangle_1' = C_{\mathrm{s}}^{-1}\left(\langle i_{\mathrm{Ls}}\rangle_1-\langle f_s i_{\mathrm{Lf}}\rangle_1\right)-j\omega_0\langle v_{\mathrm{Cs}}\rangle_1\\
\langle i_{\mathrm{Lf}}\rangle_0' = -L_{\mathrm{f}}^{-1}\left(\langle v_{\mathrm{Cf}}\rangle_0-\langle f_s v_{\mathrm{Cs}}\rangle_0\right)\\
\langle v_{\mathrm{Cf}}\rangle_0' = -C_{\mathrm{f}}^{-1}\left(\langle v_{\mathrm{Cf}}\rangle_0-R_{\mathrm{L}}\langle i_{\mathrm{Lf}}\rangle_0\right)
\end{cases} \tag{11}$$

where $\Psi=M^2-L_{po}L_s$.

In the transformation, first-order harmonic is enough to describe the dynamic behavior of the fast oscillatory variables as the LCL resonant and parallel network can eliminate high-order harmonics. However, for the slow time-varying variables, with the LC filter, the zero-order harmonic can achieve good approximation.

Two nonlinear items in (11) can be expanded by convolution of the Fourier coefficient. The results are as follows:

$$\begin{aligned}\langle f_s i_{\mathrm{Lf}}\rangle_1 &= \sum_{i=-1,0,1}\langle f_s\rangle_{1-i}\langle i_{\mathrm{Lf}}\rangle_i\\ &=\langle f_s\rangle_2\langle i_{\mathrm{Lf}}\rangle_{-1}+\langle f_s\rangle_1\langle i_{\mathrm{Lf}}\rangle_0+\langle f_s\rangle_0\langle i_{\mathrm{Lf}}\rangle_1\end{aligned} \tag{12}$$

$$\begin{aligned}\langle f_s v_{Cs}\rangle_0 &= \sum_{i=-1,0,1}\langle f_s\rangle_{0-i}\langle v_{Cs}\rangle_i\\ &=\langle f_s\rangle_1\langle v_{Cs}\rangle_{-1}+\langle f_s\rangle_0\langle v_{Cs}\rangle_0+\langle f_s\rangle_{-1}\langle v_{Cs}\rangle_1\end{aligned} \tag{13}$$

The Fourier coefficients of the nonlinear switching functions can be expressed as

$$\langle f_p\rangle_n=-\langle f_s\rangle_n=\begin{cases}0 & \mathrm{n}=0,\pm2,\pm4\cdots\\ \dfrac{-2j}{n\pi} & \mathrm{n}=\pm1,\pm3,\pm5\cdots\end{cases} \tag{14}$$

A generalized state space averaging model can be acquired by substituting (12), (13), and (14) into (11). However, the coefficients of the fast oscillatory variables include both real and imaginary parts. It is necessary to detach them for simplification of controller design. Therefore, the new state vector in the model can be described as

$$\begin{aligned}x(t)=[&\mathrm{Re}\langle i_{Lpi}\rangle_1,\mathrm{Im}\langle i_{Lpi}\rangle_1,\mathrm{Re}\langle v_{Cp}\rangle_1,\mathrm{Im}\langle v_{Cp}\rangle_1,\mathrm{Re}\langle i_{Lpo}\rangle_1,\\ &\mathrm{Im}\langle i_{Lpo}\rangle_1,\mathrm{Re}\langle i_{Ls}\rangle_1,\mathrm{Im}\langle i_{Ls}\rangle_1,\mathrm{Re}\langle v_{Cs}\rangle_1,\mathrm{Im}\langle v_{Cs}\rangle_1,\\ &\langle i_{Lf}\rangle_0,\langle u_{Cf}\rangle_0]^T\end{aligned} \tag{15}$$

where $\mathrm{Re}(\bullet)$ and $\mathrm{Im}(\bullet)$ denote the real and imaginary parts, respectively.

Assigning the DC voltage E_{DC} as input $\boldsymbol{u}$ and the load voltage v_O, which equals v_{C_f}, as output $\boldsymbol{y}$, the state space model in frequency domain can be expressed as

$$\begin{aligned}\dot{x}(t)&=Ax(t)+Bu(t)\\ y(t)&=Cx(t)+Du(t)\end{aligned} \tag{16}$$

where $\mathbf{A}\in\mathbf{R}^{n\times n},\mathbf{B}\in\mathbf{R}^{n\times1},\mathbf{C}\in\mathbf{R}^{1\times n},n=12$, and $\mathbf{D}\in\mathbf{R}$. The detailed descriptions of **A**, **B**, **C**, **D** are provided in the Appendix.

IV. Uncertainty Modeling

In the system model, the running frequency drifts away from the designed frequency because of the varying load conditions, making the frequency and load parameter in the system model to become uncertain. Therefore, the uncertain part should be detached from the system model. The variation in uncertain parameters always has a certain boundary and the uncertain parameters can be defined as

$$\begin{aligned}\omega&=\bar{\omega}(1+p_\omega\delta_\omega)\\ R_{\mathrm{L}}&=\bar{R}_{\mathrm{L}}(1+p_{R_{\mathrm{L}}}\delta_{R_{\mathrm{L}}})\end{aligned} \tag{17}$$

where the running frequency ω and the load parameter R_L are considered. $\bar{R}_L$ is the rated load, and $\bar{\omega}$ is the ZCS operation frequency under the rated load condition, which can be solved by the ZCS condition provided in (4). δ_ω, δ_{R_L} is the uncertain part that should satisfy $\|\delta_\omega\|\le1$, $\|\delta_{R_L}\|\le1$. p_ω, p_{R_L} provide the maximum magnitude of parameter variations. An upper linear fractional transformation (LFT) can be used on δ_ω and δ_{R_L}, as shown below.

$$\omega=F_U(\mathbf{M}_\omega,\delta_\omega)=\bar{\omega}+\bar{\omega}p_\omega\delta_\omega \tag{18}$$

$$R_L=F_U(\boldsymbol{M}_{R_L},\delta_{R_L})=\bar{R}_{\mathrm{L}}+\bar{R}_{\mathrm{L}}p_{R_{\mathrm{L}}}\delta_{R_{\mathrm{L}}} \tag{19}$$

Here, the constant matrix $\mathbf{M}_\omega=\begin{bmatrix}0 & \bar{\omega}\\ p_\omega & \bar{\omega}\end{bmatrix}$, and $\mathbf{M}_{R_L}=\begin{bmatrix}0 & \bar{R}_L\\ p_{R_L} & \bar{R}_L\end{bmatrix}$.

With the LFT method, all uncertain parameters in the model can be expressed with an uncertain parameters matrix.

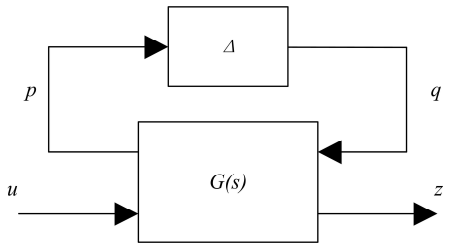

Fig. 4. Uncertain model topology.

$$\Delta = \mathrm{diag}\left\{\delta_{\omega},\cdots,\ \delta_{\omega},\delta_{R_L}\right\} \tag{20}$$

Here, $\Delta \in \mathbf{C}^{n\times n}$ is a diagonal matrix that includes all uncertain parameters and satisfies the norm condition $\left\|\Delta\right\|_{\infty} < 1$ for $\left\|\delta_{\omega}\right\| \le 1$, . $\left\|\delta_{R_L}\right\| \le 1$.

The perturbation input and output of the uncertain part can be defined as

$$q = pertin = [y_{1\omega}, y_{2\omega},\cdots, y_{10\omega}, y_{RL}]^T \tag{21}$$

$$p = pertout = [u_{1\omega}, u_{2\omega},\cdots, u_{10\omega}, u_{RL}]^T \tag{22}$$

The system model can be detached into the uncertain part Δ and into the certain part $G(s)$, as shown in Fig. 4.

Here, z is the generalized system output that considers all perturbations.

The generalized system model can be expressed as

$$\begin{cases} \dot{x} = \bar{A}x + B_1 p + B_2 u \\ q = C_1 x + D_{11} p + D_{12} u \\ z = C_2 x + D_{21} p + D_{22} u \end{cases} \tag{23}$$

In this model, the system coefficient matrix $\bar{A}$ includes only certain parameters, and the matrixes $\mathbf{B}_1$, $\mathbf{B}_2$, $\boldsymbol{C_1}$, $\boldsymbol{C}_2$, $\mathbf{D_{11}}$, $\mathbf{D}_{12}$, $\mathbf{D_{21}}$ $\mathbf{D_{21}}$, and $\mathbf{D}_{22}$ define the interconnection relationship among the system input and output.

V. μ-SYNTHESIS CONTROLLER DESIGN

In the controller design, the control target guarantees system performance under possible uncertainties. The system performance indexes include tracking error and noise rejection. On the basis of the system model provided in (23), a robust controller $u(s) = K(s)e(s)$ can be added as Fig. 5.

Here, *ref* is the reference input, and the dashed border box is the generalized plant model; *d* is the disturbance to the output with finite energy, namely, $d \in L_2$. W_p function is the performance weighting function, and W_u function is the control weighting function. $z = [e_p, e_u]^T$ is the robust performance index output. The controller should not only guarantee system internal stability but also keep the H_{∞} norm of the transfer function $T_{ds}(s)$ from perturbation input *d* to performance index below boundary γ ($\gamma > 0$).

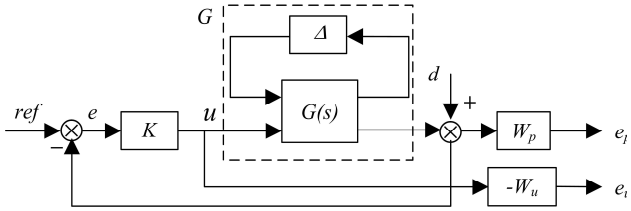

Fig. 5. Block diagram of μ-synthesis control system

$$\left\|T_{dz}(s)\right\|_{\infty} < \gamma \ , \tag{24}$$

i.e.,

$$\left\| \begin{matrix} W_p(I + F_U(G,\Delta)K)^{-1} \\ W_u K(I + F_U(G,\Delta)K)^{-1} \end{matrix} \right\|_{\infty} < \gamma \ . \tag{25}$$

The H_{∞} norm refers to the infinity norm of a transfer function.

The initial setting of W_p and W_u, W_p function reflects the dynamic system performance, which includes overshoot and settling time. The W_u function reflects the cost of control and should be below 1. Oloomi and Shafai [18] present a weight selection method to design the weighting function. In the system robust design, system un-modeled dynamics may bring system-structured uncertainty and should be considered in the controller design. Therefore, the uncertain block should be redefined to include type kind of uncertainty, which is shown as

$$\begin{cases} \underline{\Delta}(s) = diag\{\delta_1 I_{r_1},\ldots,\delta_S I_{r_S},\Delta_1,\ldots,\Delta_f\} = \begin{bmatrix} \Delta & \\ & \Delta_p \end{bmatrix} \\ \delta_i \in C, \Delta_j \in C^{m_j \times m_j} \end{cases} \tag{26}$$

.

$\boldsymbol{\Delta}$ should satisfy $B\underline{\Delta} = \{\Delta \in \underline{\Delta} : \bar{\sigma}(\Delta) \le 1\}$. $\boldsymbol{\Delta_p}$ should satisfy $\bar{\sigma}(\Delta_p) \le 1$.

The new generalized system model is shown in Fig. 6.

Here, block *P* is the total block of all open loop structures, including the generalized plant model and the weighted function; $\underline{\boldsymbol{\Delta}}$ is the uncertainty block including all unstructured and structured uncertainties.

To avoid unnecessary conservation brought by the structured uncertainty, the SSV should be adopted to evaluate the robust performance. SSV defines the smallest $\bar{\boldsymbol{\sigma}}\boldsymbol{(\Delta)}$ to make $(\mathbf{I} - \mathbf{M}\Delta)$ singular, i.e.,

$$\mu_{\Delta}(M) = \begin{cases} (\min\limits_{\Delta\in\underline{\Delta}}\{\bar{\sigma}(\Delta): \det(I - M\Delta) = 0\})^{-1}, \forall \Delta \in \underline{\Delta} \\ 0: \qquad\qquad \det(I - M\Delta) \ne 0, , \quad \forall \Delta \in \underline{\Delta} \end{cases} \tag{27}$$

In the μ-synthesis controller design, a stabilizing controller *K* should be determined and satisfy

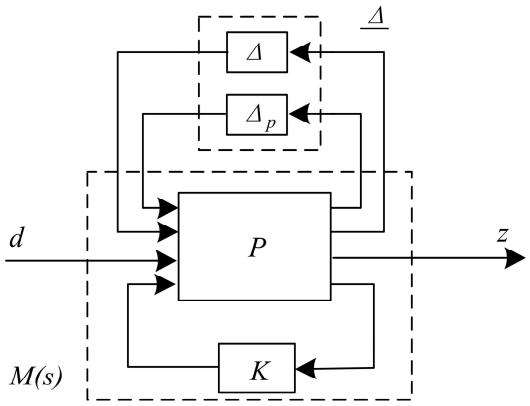

Fig. 6. Robust control system structure.

$$\sup_{\omega\in\mathbf{R}} \mu_{\underline{\Delta}}[\mathbf{M}(P,K)(j\omega)] < 1 \tag{28}$$

Furthermore, an optimal K to make the SSV minimum is necessary to achieve quality performance, i.e.,

$$\inf_{K(s)} \sup_{\omega\in\mathbf{R}} \mu_{\underline{\Delta}}[\mathbf{M}(P,K)(j\omega)] \tag{29}$$

Thus,

$$\mu_{\underline{\Delta}}[\mathbf{M}(P,K)(j\omega)] \le \bar{\sigma}[\mathbf{M}(P,K)(j\omega)] \tag{30}$$

Therefore, by using a *D–K* iteration method [17], we can express the stabilizing controller as

$$\sup_{K(s)} \inf_{D\in\underline{D}} \bar{\sigma}[DM(P,K)(j\omega)D^{-1}] < 1 \tag{31}$$

where D is the scaling matrix

$$D = \{diag(D_1,\cdots,D_s,d_1 I_{m_1},\cdots,d_f I_{m_f}): D_i \in C^{r_i\times r_i}, D_i = D_i^* > 0, d_j \in R, d_j > 0\} \tag{32}$$

D can be expressed with the norm of

$$\inf_{K(s)} \inf_{D\in\underline{D}} \left\| DM(P,K)(j\omega)D^{-1} \right\|_\infty \tag{33}$$

TABLE I
SYSTEM PARAMETERS

Parameters	Values
Inductance L_{pi} of LCL network (μH)	85.5
Capacitance C_p of LCL network (μF)	0.43
Inductance L_{po} of LCL network (μH)	159
Equivalent resistance R_{Lpi} of inductance L_{pi} (Ω)	0.115
Equivalent resistance R_{Lpo} of inductance L_{po} (Ω)	0.18
Mutual inductance M (μII)	60.9
Secondary resonant capacitance C_S (μF)	0.25
Secondary resonant inductance L_S (μH)	111.2
Equivalent resistance R_{Ls} of inductance L_S (Ω)	0.147
Load R_L (Ω)	22
Filter inductance L_f (mH)	1
Filter capacitance C_f (μF)	220

Applying the iteration method to minimize (27), the optimal $K(s)$ can be acquired. A detailed iteration process in the IPT system is described in the next section.

VI. CONTROLLER PERFORMANCE ANALYSIS

Table I lists the primary circuit parameters used in designing the LCL-resonant IPT system.

In the *D–K* iteration in the last section, $\boldsymbol{D}(s)$ is first set to unity matrix $\boldsymbol{I}$. The frequency range is set to $[10^{-2},10^{6}]$, and a feedback controller $\boldsymbol{K}(s)$ can be solved. In the first iteration, the corresponding max μ reaches 118.005, which does not satisfy the robust performance requirement. By using the solved $\boldsymbol{K}(s)$, we can acquire the scaling matrix $\boldsymbol{D}(s)$, and the solved $\boldsymbol{D}(s)$ can be used to obtain a better $\boldsymbol{K}(s)$. With the iterative computation, the solved controller $\boldsymbol{K}(s)$ finally satisfies the performance requirement provided in (31). The characteristic parameters of the controller K and the scaling matrix D in the iteration process are listed in Table II.

The maximum μ value decreases in every iteration and finally drops below 1 after four iterations. In the frequency range of $[10^{-2},10^{6}]$, the frequency response of μ is shown in Fig. 7.

In the entire frequency range, μ is always below 1. Therefore, the robust stability and performance can be satisfied. Furthermore, the permitted perturbation under the structured uncertainty condition can be expressed as

$$\|\Delta\|_\infty < 1/0.549 \tag{34}$$

The final $\boldsymbol{K}(s)$ in the iteration can be selected as a controller. However, the controller order increases to 18, which is necessary to reduce the order of the controller on the condition that the robust performance indexes are satisfied. The Hankel norm approximation method is used to reduce the controller from 18 to 7. Comparison before and after order reduction is provided in Fig. 8.

The real and dashed lines correspond to the frequency response before and after order reduction, respectively. The two frequency response curves reach a good agreement in the frequency range of $[10^{-2},10^{5}]$, which verifies the feasibility of the reduced-order controller.

VII. SIMULATION RESULTS USING GSSA MODEL

The GSSA model for the LCL-resonant system with the robust control method has been constructed by using MATLAB-Simulink. The simulation parameters are listed in Table I, and the topology of the model is shown in Fig. 9.

TABLE II
ITERATION PARAMETERS

Iteration	Controller Order	Total D-Scale Order	Max μ Value
1	14	0	118.005
2	14	0	66.639
3	14	0	2.040
4	18	14	0.549

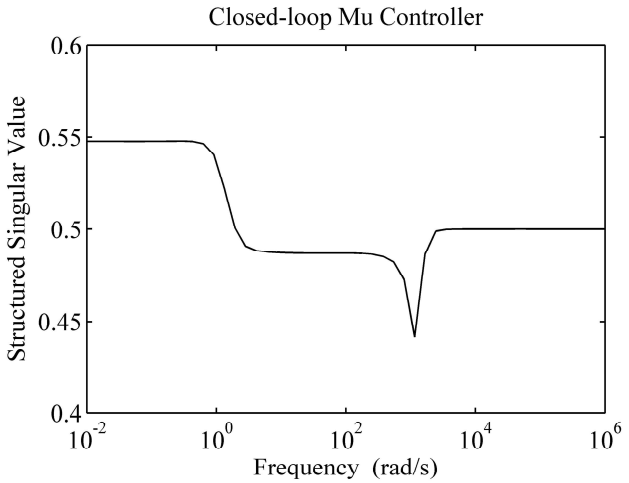

Fig. 7. Frequency response of μ.

In the simulation model, the dashed box refers to the generalized system model G with detached uncertain part. The output y of the model is affected by an external disturbance d. The error signal e is the difference between the output y and reference signal *ref*, and the controller block produces a control output u with the robust control algorithm discussed earlier.

In the model, the elements of the uncertainty matrix $\boldsymbol{\Delta}$ are replaced by a group of bounded random signal. The weighting function W_p and W_u are shown as

$$W_p(s) = \frac{1{,}000}{10s+1}$$
$$W_u(s) = 10^{-2} \quad . \tag{35}$$

The controller should be discretized to make the controller suitable for digital processing unit implementation, such as digital signal processing (DSP). Using bilinear transformation, the controller discretization can be expressed as

$$\begin{aligned} x(n+1) &= A_k x(n) + B_k u(n) \\ y(n) &= C_k x(n) + D_k u(n) \end{aligned} \quad . \tag{36}$$

The coefficient matrix can be defined as

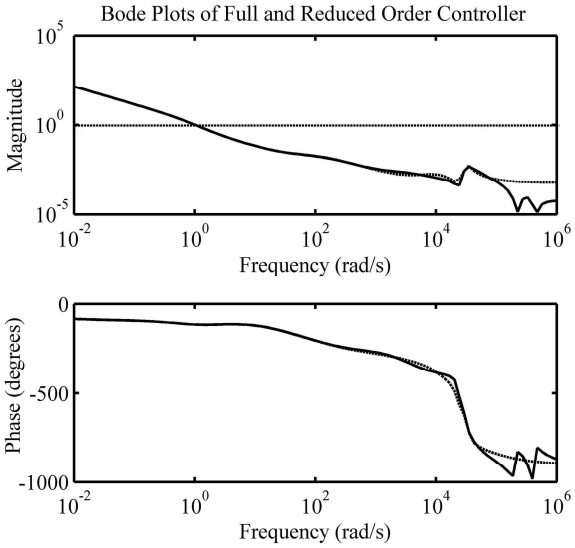

Fig. 8. Frequency response reduced-order controllers.

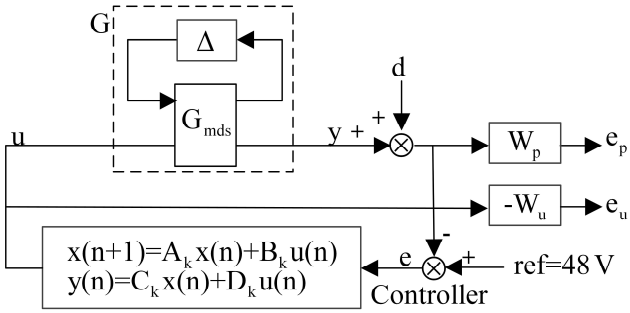

Fig. 9. Simulation model.

$$\mathbf{A}_k = \begin{bmatrix} 2.88 & -2.72 & 0.84 & 0.012 & 6.78 & -1.40\text{e-}8 & 7.44\text{e-}13 \\ 1 & 0 & 0 & 0 & 0 & 0 & 0 \\ 0 & 1 & 0 & 0 & 0 & 0 & 0 \\ 0 & 0 & 1 & 0 & 0 & 0 & 0 \\ 0 & 0 & 0 & 1 & 0 & 0 & 0 \\ 0 & 0 & 0 & 0 & 1 & 0 & 0 \\ 0 & 0 & 0 & 0 & 0 & 1 & 0 \end{bmatrix} \tag{37}$$

$$\mathbf{B}_k = \begin{bmatrix} 1 & 0 & 0 & 0 & 0 & 0 & 0 \end{bmatrix}^T \tag{38}$$

$$\mathbf{C}_k = 10^{-4} \cdot \begin{bmatrix} -8.05 & 8.09 & 8.43 & -8.29 & -1.73\text{e-}1 & -8.44\text{e-}4 & 1.46\text{e-}7 \end{bmatrix} \tag{39}$$

$$\mathbf{D}_k = [-0.000344] \quad . \tag{40}$$

To verify the performance of the controller, several simulation experiments were carried out. The first experiment was the dynamics response simulation from start to steady state with frequency perturbation. The simulation time range was set from 0 s to 0.2 s. The output voltage reference was set to 48 V. Simulation results are shown in Fig. 10.

The upper part of Fig. 10 is the added random frequency perturbation, and the lower part is the corresponding output

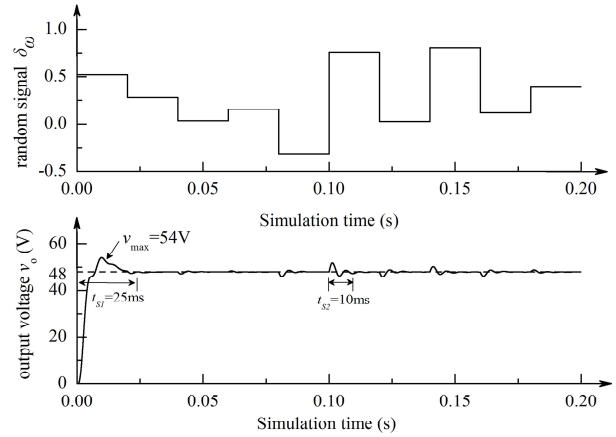

Fig. 10. Transient response under frequency perturbation.

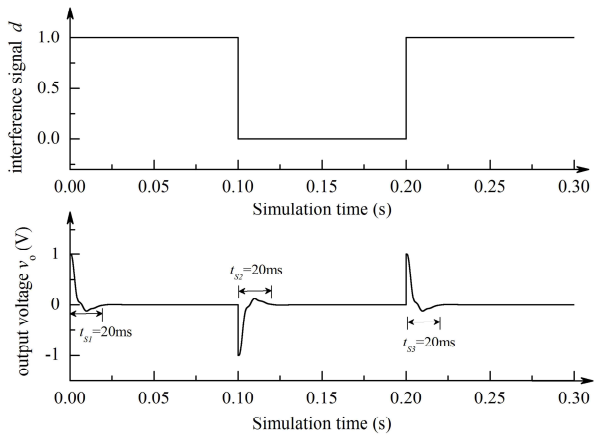

Fig. 11. Transient response under load parameter perturbation.

voltage response. From start to steady state, the settling time was 25 ms, and the system had an overshoot of about 12.5%. In the steady state, the output voltage had achieved good tracking of the reference. Furthermore, on the existence of frequency perturbation, the controller can restrain the random perturbation within 10 ms.

The second experiment was the simulation of the dynamic response with the load parameter perturbation. The simulation time range was from 0 s to 0.3 s. The reference was set to 0 to observe the controller performance without reference. A square wave signal with a period of 0.2 s was selected as the output perturbation. Simulation results are shown in Fig. 11.

The upper part of Fig. 11 is the added load parameter perturbation, and the lower part is the corresponding output voltage response. Under the perturbation, the settling time needed to track the output voltage was 20 ms. In the steady state, the output voltage can achieve a good tracking of the reference.

The third experiment was to verify the reference tracking performance of the controller. The simulation time range was from 0 s to 0.3 s. The reference was set to start at 48 V and jump to 20 V and finally return to 48 V. The reference jump instants were set to 0.1 and 0.2 s, respectively. Simulation results are shown in Fig. 12.

The output voltage had good tracking of the reference variation from 48 V to 20 V to 48 V. Tracking was completed after approximately 20 ms.

The simulation results verified that the μ controller can achieve good reference tracking and perturbation rejection performance.

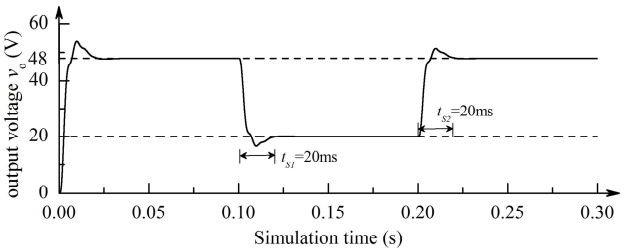

Fig. 12. Transient response with reference tracking.

VIII. PHYSICAL SYSTEM SIMULATION RESULTS

To verify the robust control method, a physical system simulation model is set up by using MATLAB. The simulation model is shown in Fig. 13.

The block of the LCL resonant IPT system refers to the entire system provided in Fig. 1. A controllable voltage source block is placed in front of the IPT system to produce a DC regulation input E_{DC}. The output voltage V_o is compared with a reference voltage to produce error signal e. The discretized robust controller produces control output u based on the error signal, and the control output u is converted to the regulation signal $\tilde{E}_{dc}$ to the controllable voltage source block.

Several simulations have been carried out to verify the controller performance. The first simulation was the dynamics response test from start to steady state. The reference voltage was set to 48 V. The simulation results are shown in Fig. 14.

The three waveforms from up to down are output voltage v_o, Buck chopper output E_{DC}, and primary resonant current $i_{L_{po}}$, respectively. From system start to steady state, the settling time was 25 ms and had a 15% overshoot. In the steady state, the system had a stable output voltage (48 V) and had a good reference tracking performance.

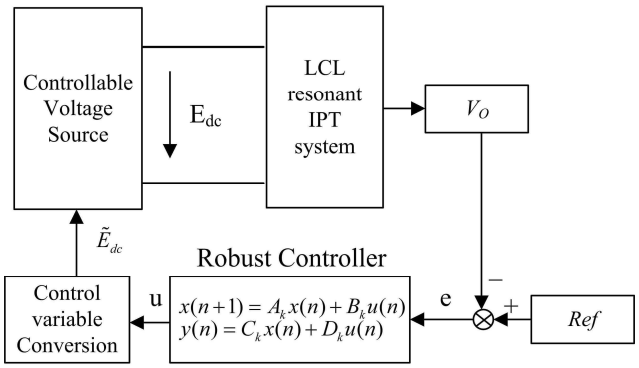

Fig. 13. Physical simulation model.

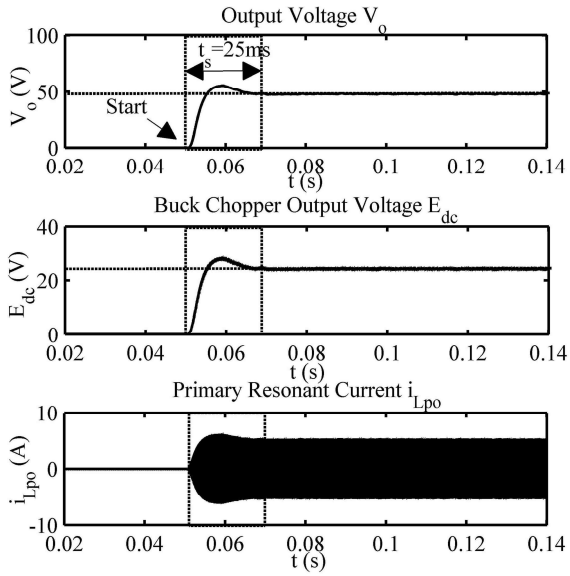

Fig. 14. System start simulation under robust control.

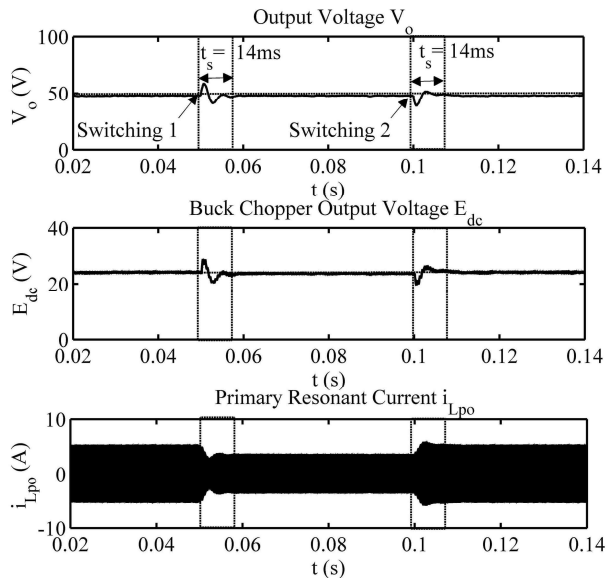

Fig. 15. Load jumping simulation under robust control.

The second simulation was the perturbation rejection test on the condition of load parameter variation. The load was switched between 22 and 33 Ω. The results are shown in Fig. 15.

The three waveforms from up to down are output voltage v_o, Buck chopper output E_{DC}, and primary resonant current $i_{L_{po}}$, respectively. Two load switching tests were used. The first switching test was the load jumps from 22 Ω to 33 Ω and the second was the load jumps back from 33 Ω to 22 Ω. In each switching, about 14 ms was needed to complete the control regulation and had a maximum 11 V overshoot on the output voltage. The Buck chopper output had a regulation between 24 and 23 V. Under load perturbation, the output voltage was always maintained at the reference voltage.

To observe the controller performance under steady state, two tests have been conducted on the condition that the load resistance was set to 22 and 33 Ω, respectively. The results are shown in Fig. 16.

The three waveforms from up to down are output voltage v_o, Buck chopper output E_{DC}, and primary resonant current $i_{L_{po}}$, respectively. On both load conditions, the output voltage was always stable with no voltage ripple. However, on the Buck chopper output, a small ripple exists because of the controller tiny regulation. The resonant current maintained sine oscillation with low distortion.

The third simulation was the verification of the reference tracking performance of the controller. The reference voltage was set to have two switches between 48 and 20 V. The results are shown in Fig. 17.

The three waveforms from up to down are output voltage v_o, Buck chopper output E_{DC}, and primary resonant current $i_{L_{po}}$, respectively. The first switching test was from 48 V to 20 V, and the second was from 20 V to 48 V. The regulation time in both switching is about 20 ms. The maximum overshoot was about 10% on the output voltage. The output voltage had achieved good tracking performance in the system dynamics.

IX. Experimental Results

For the sake of verifying the controller performance in a real LCL resonant IPT system, an experimental system has been constructed according to the parameters provided in Table I. The structure of the experimental system is shown in Fig. 18.

The block of the LCL resonant IPT system refers to the entire system given in Fig. 1. A Buck DC chopper with input voltage $U_d = 25$ V is placed in front of the IPT system. The

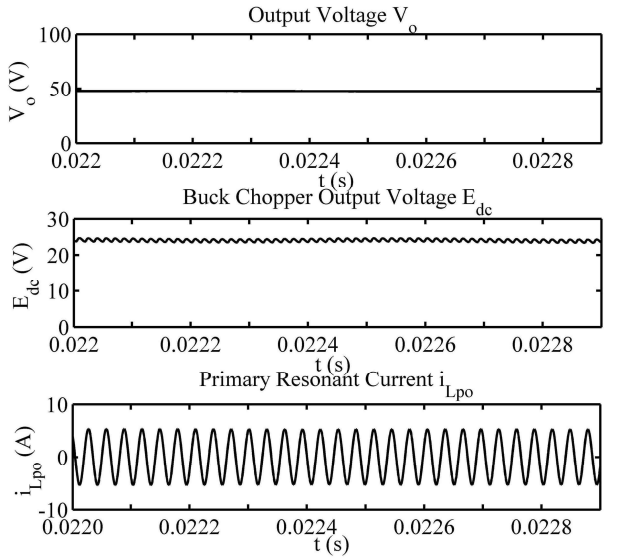

(a) $R_L = 22\Omega$

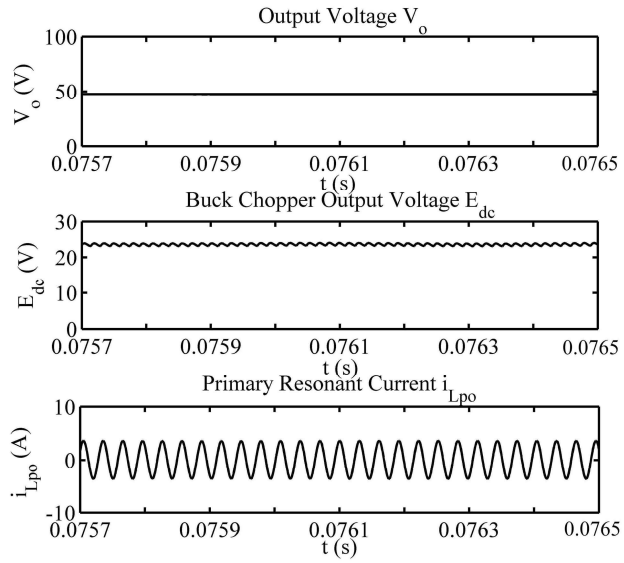

(b) $R_L = 33\Omega$

Fig. 16. System steady-state simulation.

filter inductance L_b and filter capacitance are 1 mH and 470 μF. The operation frequency is 100 kHz. The primary function of the chopper is to produce a variable DC input voltage E_{DC} regulation for the IPT system according to the robust controller output. The output voltage V_O is measured with a resistor divider network and sample by an AD574 sampling chip. The output voltage information is sent back to the primary part with the aid of a RF link. The robust μ control algorithm is embedded in the DSP unit (type: TMS320F2812). The control output is transformed into a PWM signal in the gate drive module and drives the Buck chopper to realize control.

Several experiments have been carried out for verification

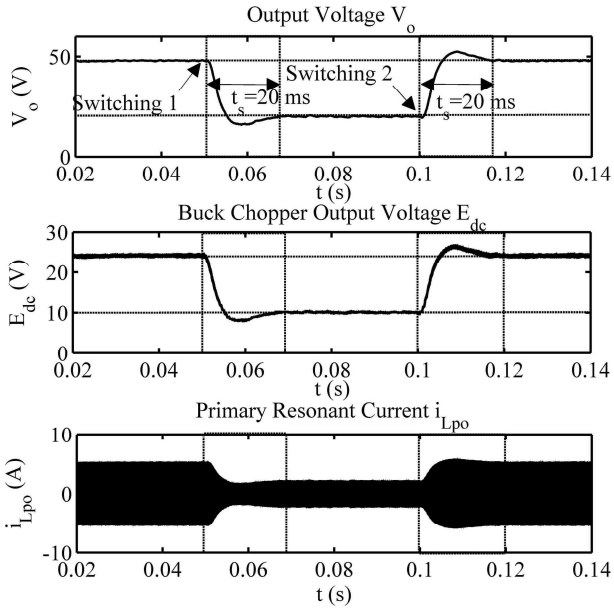

Fig. 17. Reference tracking simulation under robust control.

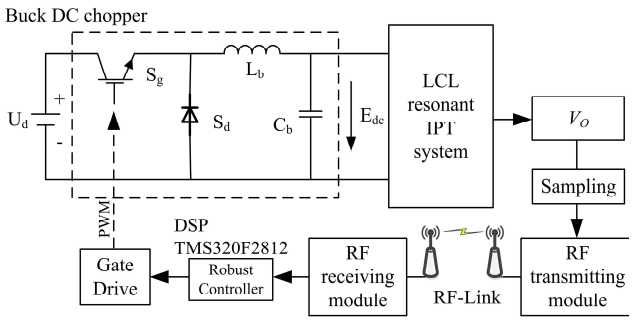

Fig. 18. Experimental system structure.

of the controller performance. The first experiment was the dynamics response test from start to steady state. The reference voltage was set to 48 V. The experiment results are shown in Fig. 19.

The three waveforms from up to down are output voltage v_o, Buck chopper output E_{DC}, and primary resonant current $i_{L_{po}}$, respectively. From system start to steady state, it took about 28 ms and no overshoot occurred in the process. In the steady state, the system had a stable output voltage (48 V), and the output voltage had achieved good tracking of the reference.

The second experiment was the perturbation rejection test on the condition of load parameter variation. The load was switched between 22 and 33 Ω. The experimental results are shown in Fig. 20.

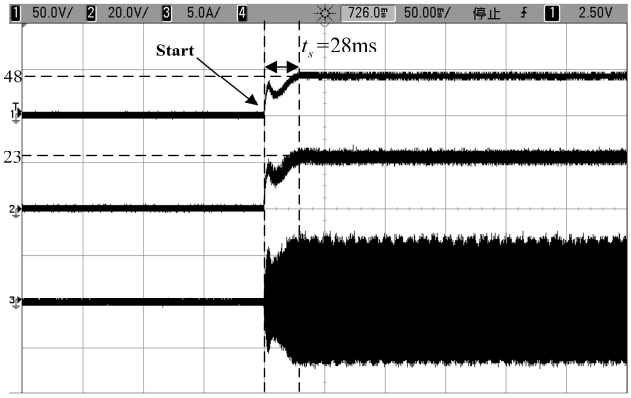

Fig. 19. System start experimental waveforms under robust control.

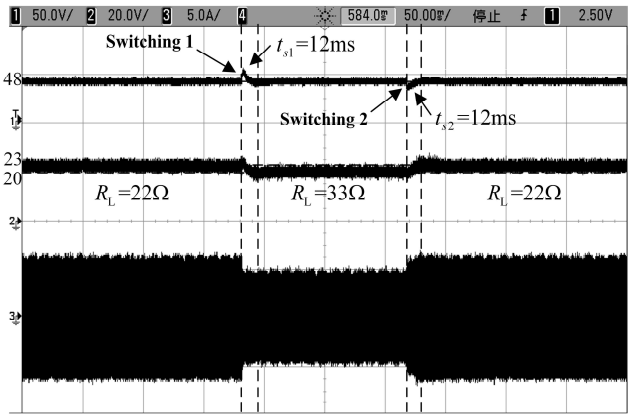

Fig. 20. Load jumping experimental waveforms under robust control.

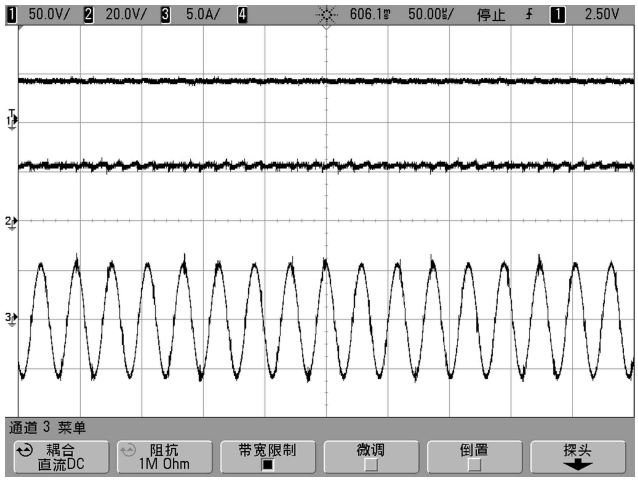

(a) $R_L = 22\Omega$

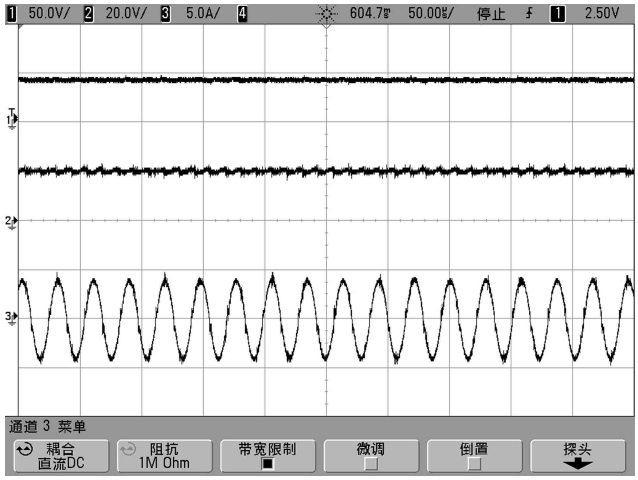

(b) $R_L = 33\Omega$

Fig. 21. System steady state experimental waveforms.

The three waveforms from up to down are output voltage v_o, Buck chopper output E_{DC}, and primary resonant current $i_{L_{po}}$, respectively. Two load switching tests were conducted. The first switching test was the load jumps from 22 Ω to 33 Ω and the second was the load jumps back from 33 Ω to 22 Ω. The settling time was 12 ms for each switching to complete the control regulation and had a max 6 V overshoot on output voltage. The Buck chopper output had a regulation between 23 and 20 V. Under load perturbation, the output voltage was always maintained at the reference voltage.

Two tests have been carried out on the condition that the load resistance was 22 Ω and 33 Ω, respectively, to observe the controller performance under the steady state. The results are shown in Fig. 21.

The three waveforms from up to down are output voltage v_o, Buck chopper output E_{DC}, and primary resonant current $i_{L_{po}}$, respectively. On both load conditions, the output voltage was always stable without voltage ripple. However, a small ripple exists on the Buck chopper output because of the controller tiny regulation. The resonant current was maintained sine oscillation with low distortion. The ZCS frequency in (a) was 34.9 kHz, and the ZCS frequency in (b) was 35.7 kHz. The frequency drifting was about 0.8 kHz. The system efficiency in (a) was 79%, and the system efficiency in (b) was 73%. The results show that the system can achieve good robust performance when the load and frequency perturbation were imposed to the system.

The third experiment was the verification of the reference tracking performance of the controller. The reference voltage was set to have two switches between 48 and 20 V. The first switching was set from 48 V to 20 V, and the second switching was set from 20 V to 48 V. The experimental results are shown in Fig. 22.

The three waveforms from up to down are output voltage v_o, Buck chopper output E_{DC}, and primary resonant current $i_{L_{po}}$, respectively. The first switching test was from 48 V to 20 V and the second was from 20 V to 48 V. The regulation time in both switching was about 30 ms. Almost no overshoot

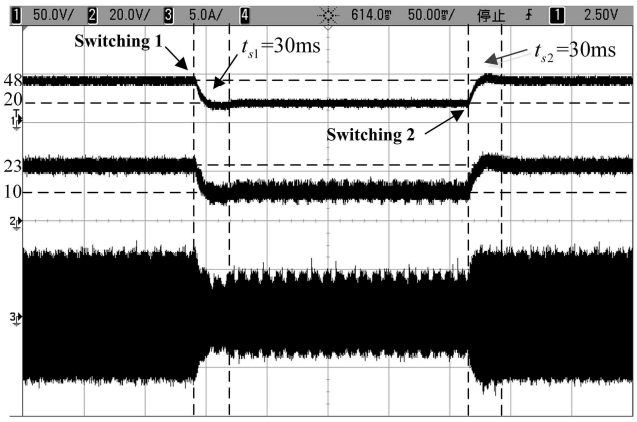

Fig. 22. Reference tracking experimental waveform under robust control.

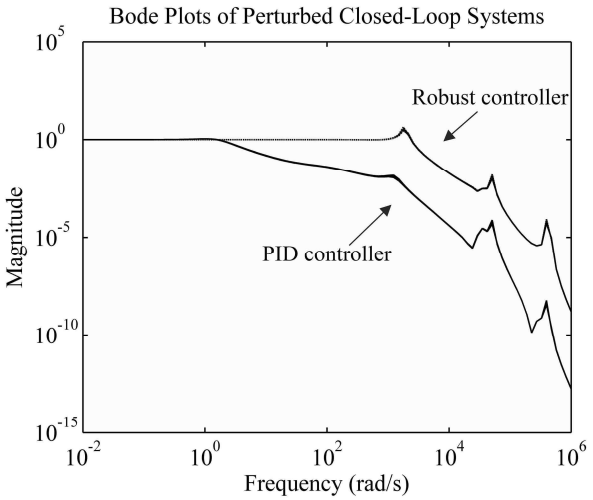

Fig. 23. Frequency response comparison between the robust and PID controller.

on the output voltage exists. The output voltage has achieved a good tracking performance in the system dynamics. However, a small ripple occurred on the envelope of the resonant current because of the tiny regulation.

X. COMPARISON

An experimental system was set up to compare the robust control method with the conventional control method. A normal PID control method was selected for comparison. The PID controller was discretized with a sampling period T = 1 μs. The PID controller is expressed as

$$T(z) = \frac{0.5\,z - 0.48}{z - 1}. \tag{41}$$

To compare the system performance under the perturbation between the robust control and the PID control method, the closed loop frequency response comparison in the entire frequency range is used (see Fig. 23).

In the frequency range [10^0 10^6], the frequency response under robust control is much lower than the frequency response under the PID control, which denotes better perturbation suppression performance of the robust control compared with the PID control for the IPT system.

The experimental system under PID control is shown in Fig. 24.

The system structure is the same as the robust control system structure shown in Fig. 18, except that the controller used the PID control algorithm. The system parameters are the same as the parameters shown in Table I.

Similar experiments were carried to compare the control performance with the robust control method. The first comparison experiment was the dynamics response test from start to steady state. The reference voltage was set to 48 V. The experiment results are shown in Fig. 25.

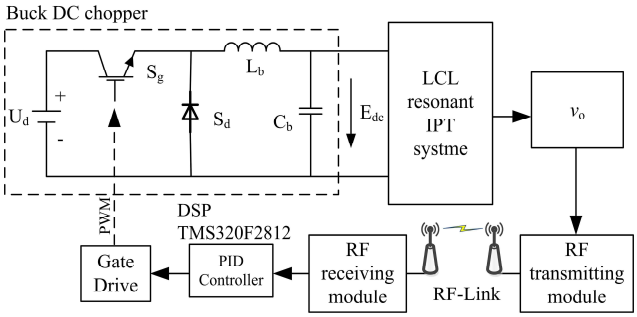

Fig. 24. Experimental system structure under conventional PID control.

The three waveforms from up to down are output voltage v_o, Buck chopper output E_{DC}, and primary resonant current $i_{L_{po}}$, respectively. Approximately 60 ms passed from start to steady state, and the system has 4 V overshoot. In the steady state, the system had a stable output voltage (48 V) and the output voltage had achieved good tracking of the reference. However, some voltage ripple exists on the Buck chopper output. Compared with the robust control, the PID control took more time to reach the reference voltage.

The second comparison experiment was the perturbation rejection test on the condition of load parameter variation. The load was switched between 22 and 33 Ω. The experimental results are shown in Fig. 26.

The three waveforms from up to down are output voltage v_o, Buck chopper output E_{DC}, and primary resonant current $i_{L_{po}}$, respectively. Two load switching tests were used. The first switching test was the load jump from 22 Ω to 33 Ω, which took about 60 ms to complete the control regulation.

The second test was the load jumps back from 33 Ω to 22 Ω, which took about 35 ms to complete the control regulation. Each switching had a maximum of 5 V overshoot on output voltage. Some ripple still exists on the Buck chopper output. The system efficiency under 22 Ω load condition was 75%, and the system efficiency under 33 Ω load condition was 69%. Compared with the robust control, the PID control takes more time to reach the reference voltage, and the system efficiency was lower than the robust control method.

The third experiment was the verification of the tracking performance of the controller. The reference voltage was set to have two switches between 48 and 20 V. The comparison experimental results are shown in Fig. 27.

The three waveforms from up to down are output voltage v_o, Buck chopper output E_{DC}, and primary resonant current $i_{L_{po}}$, respectively. The first switching test was from 48 V to 20 V and the second was from 20 V to 48 V. The regulation time in both switching was about 105 ms. Almost no overshoot on the output voltage exists. The output voltage had achieved good tracking performance in the system dynamics. However, the settling time was larger than the robust control method, and some ripple existed on the Buck chopper output.

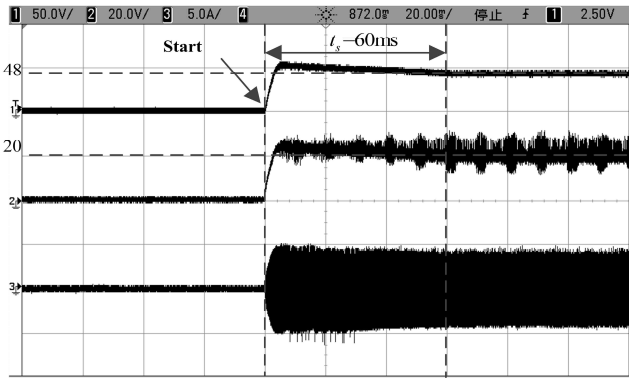

Fig. 25. System start experimental waveforms.

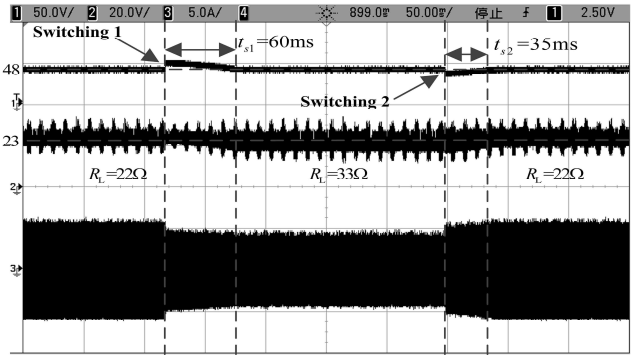

Fig. 26. Load jumping experimental waveforms under PID control.

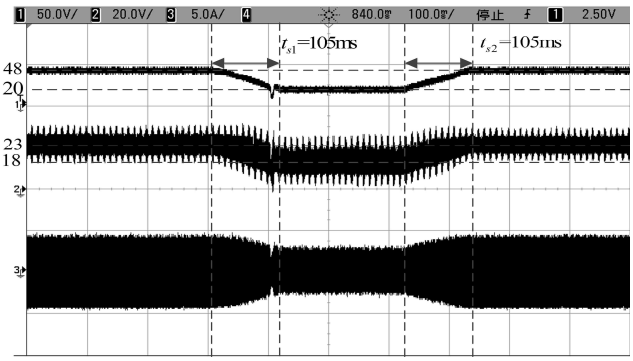

Fig. 27. Reference tracking experimental waveform under PID control.

XI. CONCLUSIONS

The IPT system is a nonlinear, high-order, and partially uncertain system. The mathematical model and the global control method of the entire system are difficult to set up. A robust optimization control method is proposed to enhance output control and to optimize the performance of the complex system. A generalized state space averaging model is constructed to transform the nonlinear model into a linear approximation model. Considering the running frequency and load parameter uncertainty, the uncertain system model is detached from the system model by using the LFT method. Taking the system stability and performance into account, a robust control structure is introduced for the LCL resonant IPT system. The weighting functions are also designed. A robust μ controller based on the SSV is designed to realize optimal control and to avoid unnecessary conservation. The detailed analysis of the controller performance is provided. Order reduction and discretization are applied on the controller for the convenience of hardware realization. The control method is verified by simulation and experimental results.

ACKNOWLEDGMENT

The research work is financially supported by the research fund of Project No. CDJZR11 17 00 01 from the Fundamental Research Funds for the Central Universities of China.

APPENDIX

The matrices A, B, C, D in (16) are listed as follows:

A=

$$\begin{bmatrix}
-L_{pi}^{-1}R_{Lpi} & \omega_0 & -L_{pi}^{-1} & 0 & 0 & 0 & 0 & 0 & 0 & 0 & 0 & 0 \\
-\omega_0 & -L_{pi}^{-1}R_{Lpi} & 0 & -L_{pi}^{-1} & 0 & 0 & 0 & 0 & 0 & 0 & 0 & 0 \\
C_p^{-1} & 0 & 0 & \omega_0 & -C_p^{-1} & 0 & 0 & 0 & 0 & 0 & 0 & 0 \\
0 & C_p^{-1} & -\omega_0 & 0 & 0 & -C_p^{-1} & 0 & 0 & 0 & 0 & 0 & 0 \\
0 & 0 & -\Psi^{-1}L_s & 0 & \Psi^{-1}L_sR_{Lpo} & \omega_0 & \Psi^{-1}MR_{Ls} & 0 & \Psi^{-1}M & 0 & 0 & 0 \\
0 & 0 & 0 & -\Psi^{-1}L_s & -\omega_0 & \Psi^{-1}L_sR_{Lpo} & 0 & \Psi^{-1}MR_{Ls} & 0 & \Psi^{-1}M & 0 & 0 \\
0 & 0 & -\Psi^{-1}M & 0 & \Psi^{-1}MR_{Lpo} & 0 & \Psi^{-1}L_{po}R_{Ls} & \omega_0 & \Psi^{-1}L_{po} & 0 & 0 & 0 \\
0 & 0 & 0 & -\Psi^{-1}M & 0 & \Psi^{-1}MR_{Lpo} & -\omega_0 & \Psi^{-1}L_{po}R_{Ls} & 0 & \Psi^{-1}L_{po} & 0 & 0 \\
0 & 0 & 0 & 0 & 0 & 0 & C_s^{-1} & 0 & 0 & \omega_0 & 0 & 0 \\
0 & 0 & 0 & 0 & 0 & 0 & 0 & C_s^{-1} & -\omega_0 & 0 & -2\pi^{-1}C_s^{-1} & 0 \\
0 & 0 & 0 & 0 & 0 & 0 & 0 & 0 & 0 & 4\pi^{-1}L_f^{-1} & 0 & -L_f^{-1} \\
0 & 0 & 0 & 0 & 0 & 0 & 0 & 0 & 0 & 0 & C_f^{-1} & -C_f^{-1}R_L^{-1}
\end{bmatrix}$$

where $\Psi = M^2 - L_{po}L_s$

$$B = [0 \quad -2\pi^{-1}L_{pi}^{-1} \quad 0 \quad 0 \quad 0 \quad 0 \quad 0 \quad 0 \quad 0 \quad 0 \quad 0 \quad 0]^T$$

$$C = [0 \quad 0 \quad 0 \quad 0 \quad 0 \quad 0 \quad 0 \quad 0 \quad 0 \quad 0 \quad 0 \quad 1]^T$$

$$D = 0$$

REFERENCES

[1] G. Elliott, S. Raabe, G. A. Covic, and J. T. Boys, "Multiphase pickups for large lateral tolerance contactless power-transfer systems," *IEEE Trans. Ind. Electron.,* Vol. 57, No. 5, pp. 1590-1598, May 2010.

[2] J. T. Boys, C. I. Chen and G. A. Covic, "Controlling inrush currents in inductively coupled power systems," in *IEEE IPEC,* Vol. 2, pp. 1046-1051, 2005.

[3] J. T. Boys, G. A. Covic and A. W. Green, "Stability and control of inductively coupled power transfer systems," in *Proc. IEE Electric Power Applications,* Vol. 147, No. 1, pp. 37-43, Jan. 2000.

[4] J. T. Boys, J. T. Boys, G. A. Covic, and X. Yongxiang, "DC analysis technique for inductive power transfer pick-ups DC analysis technique for inductive power transfer pick-ups," *IEEE Power Electron. Lett.,* Vol. 1, No. 2, pp. 51-53, Jun. 2003.

[5] N. A. Keeling, G. A. Covic and J. T. Boys, "A unity-power-factor IPT pickup for high-power applications," *IEEE Trans. Ind. Electron.,* Vol. 57, No. 2, pp. 744-751, Feb. 2010.

[6] A. P. Hu and L. L. Hao, "A new high frequency current generation method for inductive power transfer applications," in *IEEE PESC,* pp. 1-6, 2006.

[7] G. A. Covic, J. T. Boys, M. L. G. Kissin, and H. G. Lu, "A three-phase inductive power transfer system for roadway-powered vehicles," *IEEE Trans. Ind. Electron.,* Vol. 54, No. 6, pp. 3370-3378, Dec. 2007.

[8] S. Ping, A. P.Hu, S. Malpas, and D. Budgett, "A frequency control method for regulating wireless power to implantable devices" *IEEE Trans. Biomed. Circuits Syst.,* Vol. 2, No. 1, pp. 22-29, Mar. 2008.

[9] H. H. Wu, A. Gilchrist, K. Sealy, P. Israelsen, and J. Muhs, "Design of symmetric voltage cancellation control for LCL converters in inductive power transfer systems," in *IEEE IEMDC,* pp. 866-871, 2011.

[10] C. S. Tang, Y. Sun, Y. G. Su, S. K. Nguang, and A. P. Hu, "Determining multiple steady-state ZCS operating points of a switch-mode contactless power transfer system," *IEEE Trans. Power Electron.,* Vol. 24, No. 2, pp. 416-425, Feb. 2009.

[11] X. Dai and X. Huang, "Study on dynamic accurate modeling and nonlinear phenomena of a push-pull soft switched converter," in *IEEE ICIEA*, pp. 1-4, 2006.

[12] A. P. Hu, "Selected Resonant Converters for IPT power supplies," PhD. dissertation, The University of Auckland, pp. 51-52, 2000.

[13] S. Ping, A. P. Hu, S. Malpas, and D. Budgett, "Switching frequency analysis of dynamically detuned ICPT power pick-ups," in *IEEE POWERCON,* pp. 1-8, 2006.

[14] H. H. Wu, G. A. Covic, J. T. Boys, and D. J. Robertson, "A series-tuned inductive-power-transfer pickup with a controllable AC-voltage output," *IEEE Trans. Power Electron.,* Vol. 26, No. 1, pp. 98-109, Jan. 2011.

[15] H. L. Li, A. P. Hu and G. A. Covic, "Primary current generation for a contactless power transfer system using free oscillation and energy injection control," *Journal of Power Electronics,* Vol. 11, No. 3, pp. 256-262, May 2011.

[16] R.L. Steigerwald, "Comparison of half-bridge resonant converter topologies," *IEEE Trans. Power Electron.*, Vol. 3, No. 2, pp. 174-182, Apr. 1988.

[17] D. W. Gu and P. H. Petkov, *Robust Control Design with MATLAB,* Springer, New York, 2005.

[18] H. Oloomi and B. Shafai, "Weight selection in mixed sensitivity robust control for improving the sinusoidal tracking performance," in *IEEE CDC*, Vol. 1, pp. 300-305, 2003.

Xin Dai received his B.E. in Industrial Automation from Yuzhou University, Chongqing, China, in 2000. He received his Ph.D. in Control Theory and Control Engineering from the School of Automation, Chongqing University, Chongqing, China, in 2006.

In 2012, he was a visiting scholar in the University of Auckland, New Zealand. He is currently working as a professor in the School of Automation, Chongqing University. His current research interests include inductive power transfer technology and nonlinear dynamic behavior analysis of power electronics.

Yang Zou received his BS in Mathematics and Applied Mathematics in 2007 from the School of Mathematics and Statistics, Chongqing University, Chongqing, China. He is currently pursuing his M.S. degree in Control Theory and Control Engineering at the School of Automation, Chongqing University, Chongqing, China. His current research interests include robust control theory, inductive power transfer technology, and nonlinear dynamic behavior analysis of power electronics.

Yue Sun received his B.E. in Electrical Engineering, his M.E. in Industry Automation and his Ph.D. in Mechanical Electrical Integrated Manufacturing from Chongqing University, Chongqing, China, in 1982, 1988, and 1995, respectively.

In 1997, he was a senior visiting scholar in the University of Valenciennes, France. He is currently a professor in the School of Automation, Chongqing University. His current research interests include automatic control, wireless power transfer, and power electronics applications.